Austrian Journal of Earth Sciences | Vienna | 2024 | Volume 117 | 195–206 | DOI: 10.17738/ajes.2024.0012

Geochemical aspects on formation processes of vein-hosted pyrite in the Carboniferous-Permian rocks of the Karavanke/Karawanken tunnel, northwestern Slovenia

Aleš Šoster[1*], Viktor Bertrandsson Erlandsson[2)], Mihael Ravnjak[3)]

[1)] University of Ljubljana, Faculty of Natural Sciences and Engineering, Aškerčeva c. 12, SI-1000 Ljubljana, Slovenia, ales.soster@ntf.uni-lj.si

[2)] Montanuniversität Leoben, Chair of Geology and Economic Geology, Peter Tunner Straße 5, AT-8700 Leoben, Austria, viktor.erlandsson@unileoben.ac.at

[3)] DRI Investment management Ltd., Kotnikova ul. 40, SI-1000 Ljubljana, Slovenia, mihael.ravnjak@dri.si

[*)] Corresponding author: ales.soster@ntf.uni-lj.si

Keywords: Pyrite, Geochemistry, Trace elements, Sulfur isotopes, Karawanken tunnel

Abstract

The Carboniferous-Permian organic-rich shale in the Karavanke/Karawanken tunnel exhibits extensive pyrite mineralization in the form of veins and impregnations. Significant thermal alteration, induced by the overlying Mesozoic rock sequences, led to the decomposition of organic matter into methane, which subsequently acted as a sulfate-reducing agent. The primary source of sulfate were the evaporitic layers hosted within the Paleozoic strata. Reduced sulfur species necessary for pyrite formation were produced through methane-mediated thermochemical sulfate reduction, catalyzed by specific cations (Ni^{2+}, Fe^{2+}) and clay minerals (montmorillonite). The mineralizing fluids originated from the expulsion of interstitial water and possibly from dehydration reactions related to the gypsum-to-anhydrite phase transition. The geochemical data indicate that the metals originated from the surrounding sedimentary rocks. These mineralizing fluids were characterized by low temperatures (< 300–350 °C), moderate reducing conditions, and low chlorinity. The low permeability of Carboniferous-Permian rocks, combined with the low trace element content of the investigated pyrite, mitigates the potential risk of environmental pollution.

1. Introduction

The Karawanken International Highway Tunnel, situated in northwestern Slovenia (Fig. 1a), connects the A2 Karavanke/Karawanken–Obrežje highway in Slovenia with the A11 Villach-Karawanken highway in Austria. The western tube of the tunnel, comprising a mined length of 7864 m (totaling 8019 m from portal to portal), was completed in 1991, covering 3750 m on the Slovenian side. Construction of the eastern tube, currently underway as of 2024, will span a total of 7948 m. The Slovenian section of this tube, extending to the Austrian border, measures 3546 m.

The geology of the Karawanken tunnel is lithologically and structurally complex. In its Slovenian segment, the tunnel traverses Late Carboniferous, Permian, and Triassic formations, along with Quaternary slope and glacial sediments (Buser, 1975). The Paleozoic strata consist of shale, sandstone, and conglomerates intercalated with gypsum and anhydrite beds and lenses, known to harbor significant methane concentrations (Buser, 1975; Ločniškar, 2022). In contrast, Mesozoic formations are predominantly composed of carbonates (Buser, 1975; Budkovič, 1999). Within the excavation zone of the eastern tube, specifically at tunnel chainage 2548.8-2550.7 m, the extensive pyrite veins and impregnations have been identified within the lithological unit of Carboniferous-Permian organic-rich shale. The geochemical characteristics and genesis of pyrite occurrences within the

Karawanken Tunnel remain up to this point largely unexplored and unreported.

Pyrite, the cubic iron disulfide (FeS_2), is the predominant sulfide mineral within the Earth's crust. Its trace element and isotopic composition signatures are increasingly utilized as geochemical indicators of its formation environment (Steadman et al., 2021). This is because the geochemical and isotopic composition of pyrite is influenced by subtle changes in the physicochemical conditions during its formation, such as variations in temperature, pressure, and fluid composition. Consequently, its geochemical signature provides valuable records reflecting the prevailing conditions at the time of its precipitation (Large et al., 2009, 2013; Cook et al., 2016; Steadman et al., 2021). Hence, studying geochemical composition of pyrite can contribute to recreation of diagenetic and hydrothermal histories of host-rock sequences. Additionally, the recognition and analysis of pyrite and its trace element composition hold significant importance for two primary reasons. Firstly, infrastructure such as tunnels disrupts the integrity of rocks, enabling water and oxygen to initiate the oxidation of pyrite. This process releases low pH and high sulfate fluids, which can lead to corrosive damage to concrete structures and steel (Liao et al., 2020; Brandão Capraro et al., 2021). Secondly, pyrite oxidation can contribute to the generation of acid mine drainage, potentially releasing harmful elements into both the environment and groundwater (Evangelou and Zhang, 1995; Tu et al., 2022). This consideration is particularly crucial during the construction of structures in rock formations lacking natural acid-buffering capacity, such as siliciclastic rocks and notably organic-rich shales, which are recognized for their high pyrite content (Gregory et al., 2015; Liao et al., 2020). This is due to the crucial role that organic compounds play in the complexation, transportation, and precipitation of metals (Disnar and Sureau, 1990; Tribovillard et al., 2006; Gregory et al., 2015; Liang et al., 2024).

In this study, we undertook a detailed petrographic analysis of the pyrite veins and employed *in-situ* geochemical techniques alongside sulfur isotope analyses of pyrite. These analyses were utilized in deciphering the mechanisms and processes governing the formation of the pyrite-bearing veins. Specifically, our aim was to discern the origins and chemical compositions of mineralizing fluids, while also investigating the potential roles of organic matter (including methane) and evaporites in the formation of pyrite.

2. Geological setting

Parts of southern Austria, northeastern Italy, and north-central Slovenia belong to the tectonic unit of the Southern Alps (Fig. 1a). The Southern Alps are bound to the north by the Periadriatic Fault System, which separates them from the Eastern Alps, while their southern boundary with the Dinarides is marked by the South Alpine Thrust Fault (Placer, 2008; Vozárová et al., 2009; Schmid et al., 2020). The Southern Alps encompass the Southern Karawanken, Julian, and Carnic Alps and Dolomites. The Southern Alps are composed of Paleozoic and Mesozoic rocks which reflect the transition between Variscan and Alpine orogenic cycles and record important regional geologic events predominantly associated with the formation and subsequent disassembly of the Pangea supercontinent (Devonian-Late Triassic, e.g. Stampfli et al., 2013).

The study area is stratigraphically situated in the Southern Karawanken unit of the Southern Alps. The lithological sequence of the Southern Karawanken around the Karawanken tunnel consists of Late Paleozoic and Early Mesozoic carbonate and clastic rocks (Fig. 1b). The oldest rocks in this area belong to the Late Carboniferous Auernig Formation (C_3), which was deposited unconformably on the Variscan basement, composed of Early Carboniferous flysch-like sedimentary rocks of the Hochwipfel Formation (Ebner et al., 2008). The Auernig Formation comprises quartz conglomerate, sandstone, shale with horizons of fusulinid and algal limestone, reaching a total stratigraphic thickness of 600 meters (Buser, 1975; Bauer, 1981). The Early to Middle Permian ($P_{1,2}$) is characterized by thick sequences of clastic and carbonate rocks belonging to the Trogkofel Group (Krainer, 1992, 1993; Novak, 2007). The Permian beds within the Trogkofel Group comprise quartz conglomerates, sandstones, and shales interbedded with mounds of massive reefal limestones (Buser, 1975; Novak and Skaberne, 2009; Novak and Krainer, 2022). This formation reaches a stratigraphic thickness of over 600 meters (Buser, 1975). The Middle Permian period is characterized by the Gröden Formation (P_2), consisting of red terrestrial conglomerate, sandstone, siltstone, shale, and evaporites deposited in fluvial, playa lake, and shallow marine environments (Buggisch, 1978; Ori and Venturini, 1981; Farabegoli et al., 1986; Vozárová et al., 2009). The Gröden Formation transitions vertically into the Late Permian Žažar Formation (P_3), which is considered the stratigraphic equivalent of the Bellerophon Formation (Skaberne et al., 2009). The Žažar Formation differs from the Bellerophon Formation in that the Žažar Formation is limestone-dominated, while the Bellerophon Formation is dominated by dolostone (Ramovš, 1958). The Žažar Formation is characterized by the deposition of evaporites within the Sabkha facies, with a subsequent vertical transition into bituminous limestone, dolostone, and mudstone, indicative of the restricted shelf environment (Vozárová et al., 2009; Skaberne et al., 2009). The Triassic begins with the deposition of Early Triassic (T_1) marly limestone, dolostone, marly shale, and sandstone, followed by Middle Triassic (Anisian-Ladinian) dolostone and limestone with chert (T^1_2). The Late Triassic includes Carnian limestones and dolostones (T^1_3) and Norian-Rhaetian Dachstein limestones (T^{2+3}_3) (Buser, 1975; Dozet and Buser, 2009; Ogorelec, 2011). Oligocene (Ol) sandstones, marls, and conglomerates, which structurally belong to the Pannonian Basin unit, are deposited on the Southern Alpine basement (e.g., Placer, 2008).

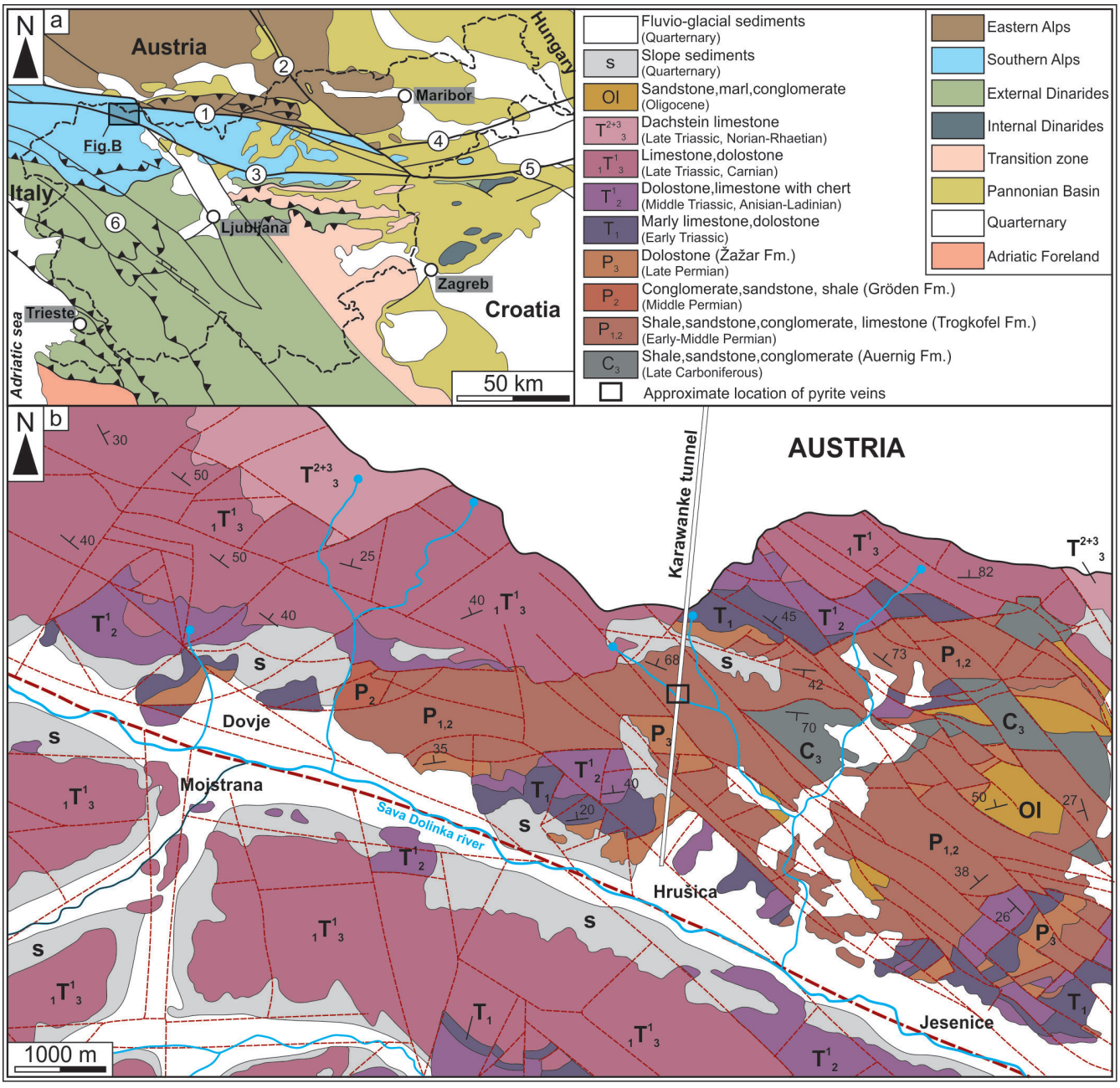

Figure 1: Geological overview of the Study Area. **(a)** Position of the research area within the regional geological context (modified after Placer, 2008). **(b)** Geological map with lithological features of the area surrounding the Karawanken tunnel. (1) Periadriatic fault, (2) Lavanttal fault, (3) Sava fault, (4) Ljutomer fault, (5) Donat fault, (6) Idrija fault. Maps adapted and modified after Buser (1975) and Placer (2008).

2.1. Geology of the Karawanken tunnel

The Karawanken tunnel is situated in northwestern Slovenia, specifically within the Southern Karawanken mountains, near the city of Jesenice, approximately 60 kilometers northwest of the Slovenian capital, Ljubljana. The geological architecture of the Karawanken tunnel is summarized and adapted from publicly available data provided by DARS (Company for Highways in the Republic of Slovenia, June 2024). At the South portal, the lithological sequence begins with 287 m of Quaternary glacial moraine and slope sediments, primarily comprising unconsolidated gravel, silt, and boulders. After passing Quaternary sediments, the tunnel enters the Early Triassic formation (287–922 m), characterized by bedded marly limestone containing lenses of gypsum and anhydrite. The Early Triassic formation is in tectonic contact with Early- to Mid-Permian units (922–1491 m) which consist of light grey to orange massive limestone (Trogkofel Fm.), carbonate breccia with red cement (Traviso breccia), and successions of quartz conglomerate, red sandstone, siltstone, with lenses of limestone, thick-bedded dolostone, and gypsum (Gröden Fm.). This formation contains

small concentrations of methane. Subsequently, the Late Carboniferous to Early Permian rocks, also referred to as the Carboniferous-Permian formation (1491–2610 m), are composed of interchanging beds of siltstone, black shale, quartz conglomerate sandstone, and limestone. This formation is characterized by high concentrations of methane. At the chainage 2610 m the Carboniferous-Permian unit is in tectonic contact with Triassic carbonates (2610–3446 m), occurring as bedded limestone and dolostone with lenses of gypsum and anhydrite. At 3466 m, the tunnel reaches the Austrian-Slovenian state boundary.

3. Materials and methods

The specimens analysed in this study were taken from the left flank of a bench located at tunnel chainage 2550.7 m. There was notable structural disparity between the left and right flanks of the bench, delineated by a tectonic contact marked by a fault (Fig. 2a). The left flank exhibited extensive mineralization by pyrite veins (Fig. 2b) within a highly deformed shale, featuring numerous rounded, pressed-in blocks and fragments of limestone. In contrast, the right flank displayed west-dipping shale beds devoid of any mineralization. The rocks in this area are classified as Carboniferous-Permian due to the challenge in distinguishing between clastic rocks of the Late Carboniferous Auernig Formation and Early Permian Trogkofel Formation without thorough paleontological analysis of intercalated limestones. A total of eight samples were prepared from the collected material, comprising five polished slabs and three polished thin sections intended for analysis with optical and scanning-electron microscopes. A sample deemed representative based on detailed petrographic analysis was selected for geochemical analyses using laser ablation inductively coupled plasma mass spectrometry (LA-ICP-MS).

3.1. Scanning-electron microscopy

The microstructures of the samples were analyzed using the ThermoFischer Scientific Quattro S field emission scanning electron microscope (FEG-SEM) equipped with an Oxford Instruments 64 energy-dispersive spectrometer (EDS). The instrument was operated under high vacuum conditions, 15 kV accelerating voltage and 10 nA beam current. Prior to analysis, the samples were coated with a thin film of amorphous carbon to ensure electrical conductivity of the sample surface and prevent charge build-up. Elemental analysis was performed at a working distance of 10 mm and a spectra acquisition time of 60 s for each measurement. The SEM analyses was done at the Department of Geology, Faculty of Natural Sciences and Engineering, University of Ljubljana, Slovenia.

3.2. Laser ablation inductively coupled plasma mass-spectrometry (LA-ICP-MS)

In-situ spot analyses of pyrite were done using an ESI NWR213 Nd:YAG laser ablation system coupled to an Agilent 8800 triple quadrupole ICP-MS, at the Chair of Geology and Economic Geology, Montanuniversität Leoben, Austria. Spot analyses had a diameter of 50 µm, with a repetition rate of 10 Hz and an on-phase laser fluency of 2–3 J/cm^2 was maintained throughout the measurements. Helium was used as the carrier gas, at a flow rate of 0.75 L/min. Measured masses: ^{34}S, ^{51}V, ^{52}Cr, ^{55}Mn, ^{57}Fe, ^{59}Co, ^{60}Ni, ^{63}Cu, ^{67}Zn, ^{71}Ga, ^{74}Ge, ^{75}As, ^{82}Se, ^{95}Mo, ^{107}Ag, ^{111}Cd, ^{115}In, ^{118}Sn, ^{121}Sb, ^{125}Te, ^{197}Au, ^{201}Hg, ^{205}Tl, ^{208}Pb and ^{209}Bi. The in-house MUL-ZnS1 was used as the primary reference material (Onuk et al. 2017), whilst the USGS MASS-1 (Wilson et al. 2002) was used for quality control and for the quantification of Te, Au, Tl and Hg – elements not present or suitable for quantification using the MUL-ZnS1. Data reduction of the raw data was done using the Iolite 4 software (Panton et al. 2011), with S as the internal standard.

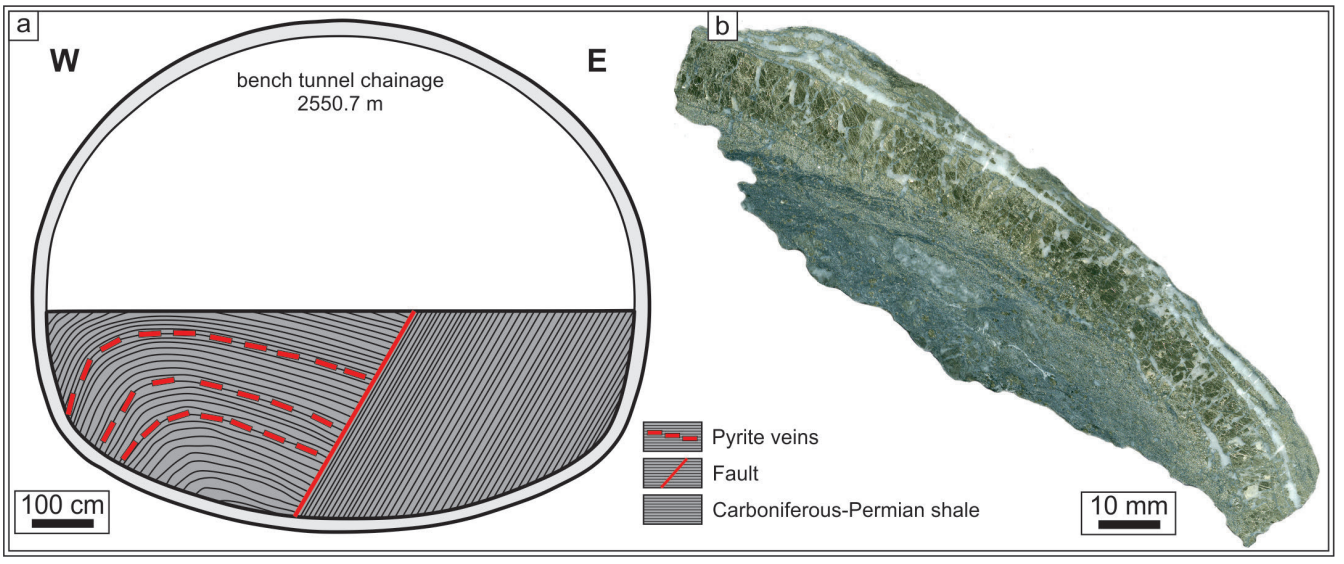

Figure 2: (a) Schematic representation of the outcrop at the pyrite mineralization site located at tunnel chainage 2550.7 meters. **(b)** The hand-sized pyrite vein specimen obtained from the Karawanken Tunnel.

3.3. Sulfur isotope analysis

The pyrite samples were handpicked from crushed rock and subsequently ground to achieve an analytical grainsize. The sulfur isotope composition of the pyrite samples was determined using the IsoPrime 100 stable isotope spectrometer and the PYRO cube elemental analyzer. Vanadium pentoxide (V_2O_5) was added to the pyrite powder prior to analysis to facilitate the combustion required to convert the sulfur in the pyrite to gaseous form for isotopic analysis. The results were calibrated to the VCDT (Vienna Canyon Diablo Troilite) scale by using the following standard reference materials: IAEA S-1, IAEA S-2, and IAEA-S3. The sulfur isotope analyses were carried out at the Environmental Department (O-2) of the Jozef Stefan Institute, Ljubljana, Slovenia.

4. Results

4.1. Vein petrography

The pyrite veins occur within highly tectonically deformed, organic-rich Carboniferous-Permian shale (Fig. 2a). The veins are arranged as discontinuous domino-like arrangements, resembling decimeter-scale boudinage structures. The pyrite veins are oriented parallel to the bedding of the intensely deformed and folded shale and can extend up to 200 mm in length and achieve a thickness of approximately 20 mm (Fig. 2b). Macroscopically, the pyrite veins exhibit a symmetrical, banded texture (Fig. 3a–c). The peripheral zones of the veins display discontinuous bands of finer-grained pyrite, reaching thicknesses of up to 4 mm. In contrast, the innermost zone is characterized by a band of coarse-grained blocky pyrite. The surrounding host rock contains numerous small, well-formed euhedral grains of diagenetic pyrite, with crystals measuring up to 400 µm in diameter and displaying cubic or octahedral shapes (Fig. 3d).

The pyrite underwent subsequent dissection and fracturing. The fractioning occurred in three distinct orientations relative to the bedding: (1) parallel, (2) perpendicular and (3) oblique orientation. The resulting cavities were then filled with different types of hydrothermal cements. The veins perpendicular to the bedding, denoted as V2 (see chapter 4.2.), exhibit symmetric syntaxial structure (*sensu* Passchier and Trouw, 2005). Their infill consists of curved fibers of quartz (Qtz1) followed by calcite (Cal) infill (Fig. 4a–b). In contrast, the parallel veins (V3), which intersect the perpendicular veins (Fig. 4c), are predominantly filled with blocky quartz (Qtz2). Lastly, the oblique veins (V4; Fig. 4d–e), intersecting both perpendicular and parallel veins contain an infill in the form of combination of barite and celestine (Brt-Cel) solid solution series, forming Ba-rich and Sr-rich bands (Fig. 4f).

4.2. Mineral paragenesis

Based on petrographic observations and cross-cutting mineral relationships, the formation of the pyrite and veins in the Carboniferous-Permian beds of the Karawanken tunnel can be divided into five stages (Fig. 5). The Stage 1 occurred during the diagenesis and is marked

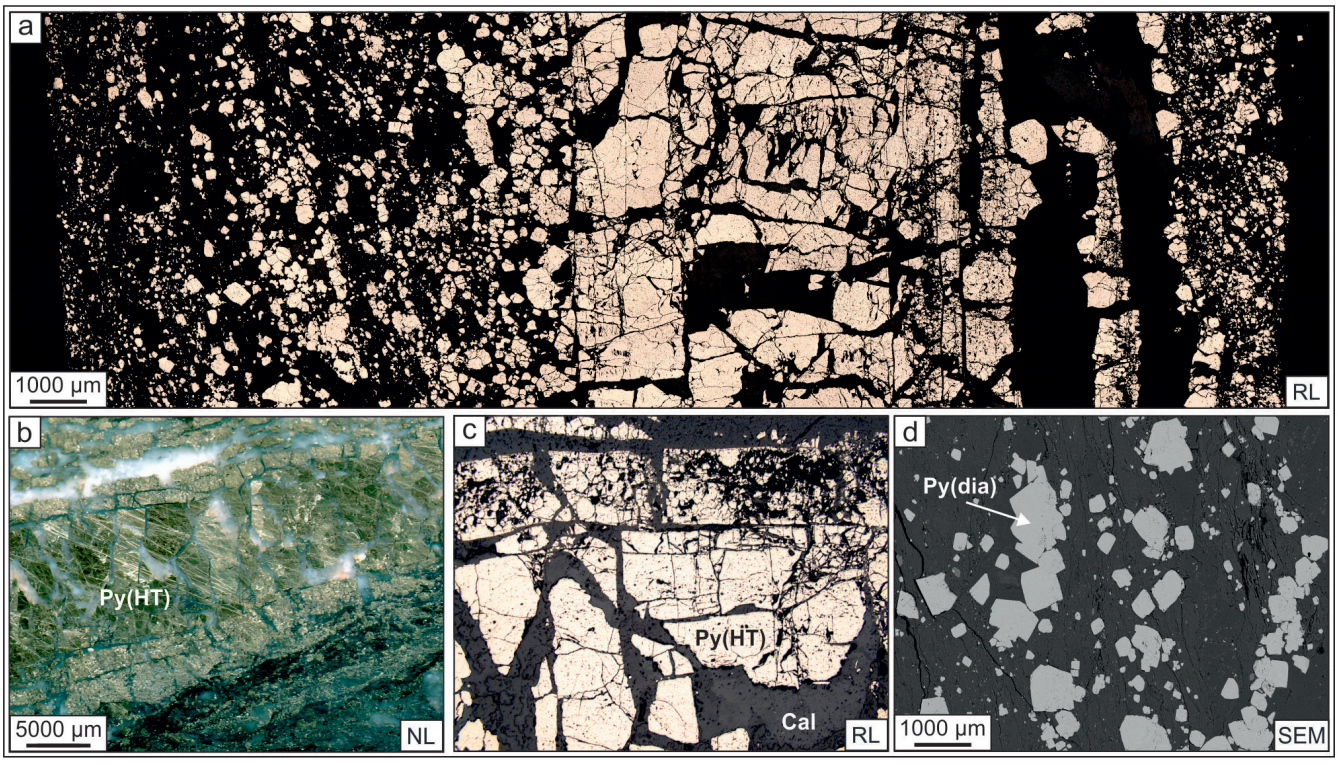

Figure 3: (a, b) Sample-scale representation and **(b-d)** principal texturer of vein pyrite (Py) from Karawanken tunnel. Py(HT): hydrothermal pyrite, Py(dia): diagenetic pyrite, RL: reflected light, NL: normal light, SEM: scanning-electron microscope (backscattered-electron imaging).

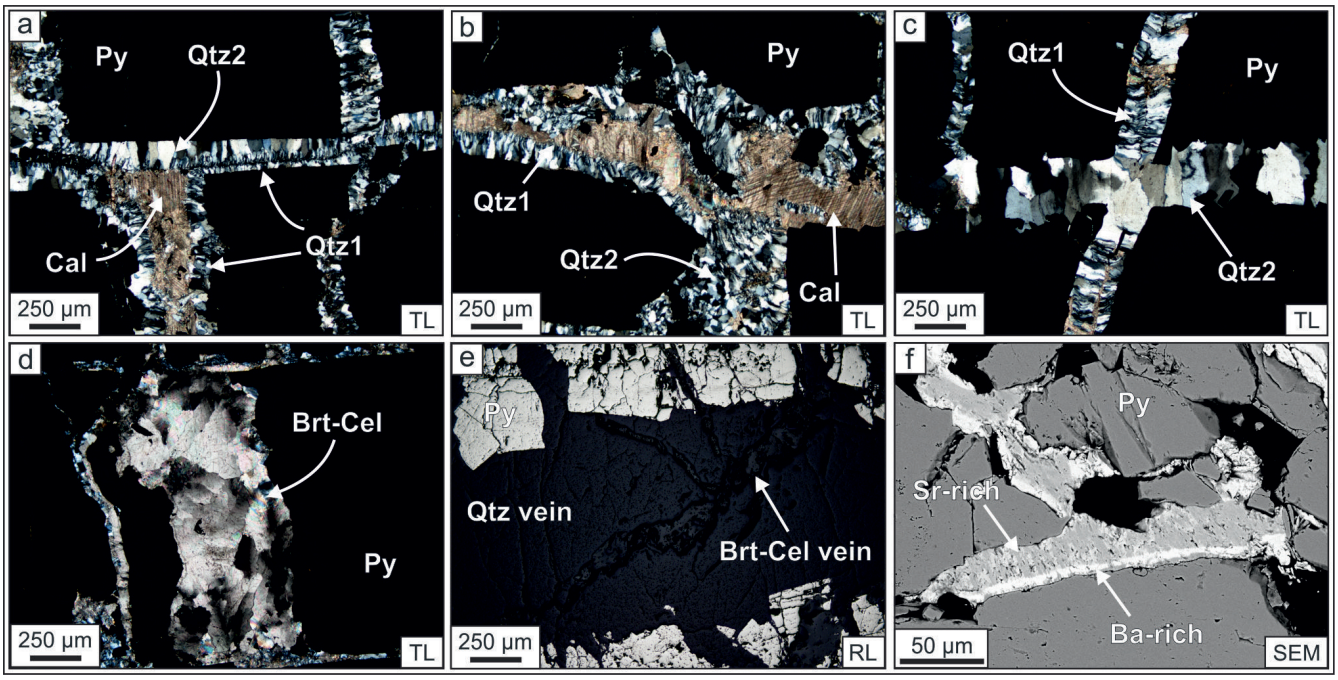

Figure 4: Microstructural characteristics of vein-infill minerals between fragmented pyrite. Py: pyrite, Qtz: quartz, Cal: calcite, Brt: barite, Cel: celestine. TL: transmitted light, RL: reflected light, SEM: Scanning-electron microscope (backscattered-electron imaging).

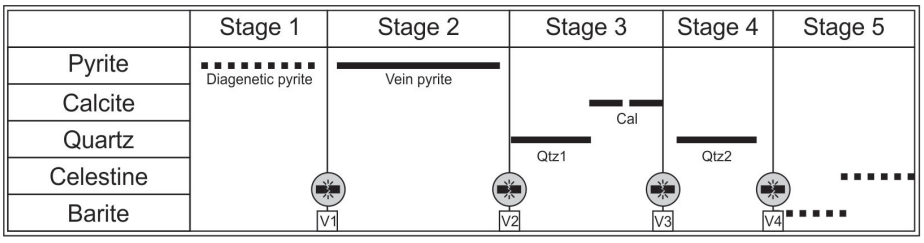

Figure 5: Paragenetic diagram depicting the mineral precipitation sequence in the Karawanken pyrite veins.

by the precipitation of early to late diagenetic pyrite. In the Stage 2, there was the precipitation of vein pyrite (V1). Whether the vein pyrite precipitated independently, or alongside other gangue minerals, remains unclear as primary mineral assemblage is likely overprinted by subsequent fracturing and mineral precipitation. Stage 3 is characterized by the formation of V2 veins and precipitation of the first-generation quartz (Qtz1) and calcite (Cal). It is likely that Qtz1 and Cal did not precipitate simultaneously; rather, calcite likely filled the remaining cavities between fractured pyrite grains and Qtz1. As calcite does not intersect Qtz2, it can be inferred that its precipitation occurred somewhere between the formation of first- and second-generation quartz. In Stage 4, bedding parallel veins (V3) formed, characterized by the precipitation of blocky quartz (Qtz2), intersecting the V2 veins. Finally, Stage 5 involved the formation of oblique veins (V4) and the precipitation of minerals from the barite-celestine solid-solution series. Based on the Brt-Cel relationship, we assume that the fluid was initially more enriched in Ba and later it became progressively enriched in Sr (Fig. 5), resulting in chemical zoning between the two in the deposited cement (e.g. Fig. 4f).

4.3. Trace element and sulfur isotope composition of pyrite

The statistical summary for the concentrations of minor and trace elements of the vein-pyrite are detailed in Table 1 and graphically presented as box-and-whisker plots in Figure 6. The vein-hosted pyrite is generally low in trace elements, however it displays elevated contents of specific elements, notably Ni (3.20–680 mg kg^{-1}), Se (2.30–8.50 mg kg^{-1}), Pb (21.5–300 mg kg^{-1}), As (5.70–197 mg kg^{-1}), and Co (0.45–99.4 mg kg^{-1}). Additionally, those elements often exhibit wide ranges of concentrations, resulting in high standard deviations (Tab. 1). This may indicate the presence of compositional zoning within the pyrite. Other elements, for example, V, Cr, Mn, Zn, Sb and Hg occur in the investigated pyrite at concentrations approximately around 10 mg kg^{-1}. While contents of Mo, Te, Bi, Ag and Au were always near or below the detection limit (Appendix 1). The analyzed samples of the vein-hosted pyrite display positive homogenous sulfur isotope composition ($\delta^{34}S$), ranging from +10.2 to +10.5 ‰ (± 0.3–0.5) with the median value of +10.4 ‰ (Tab. 2).

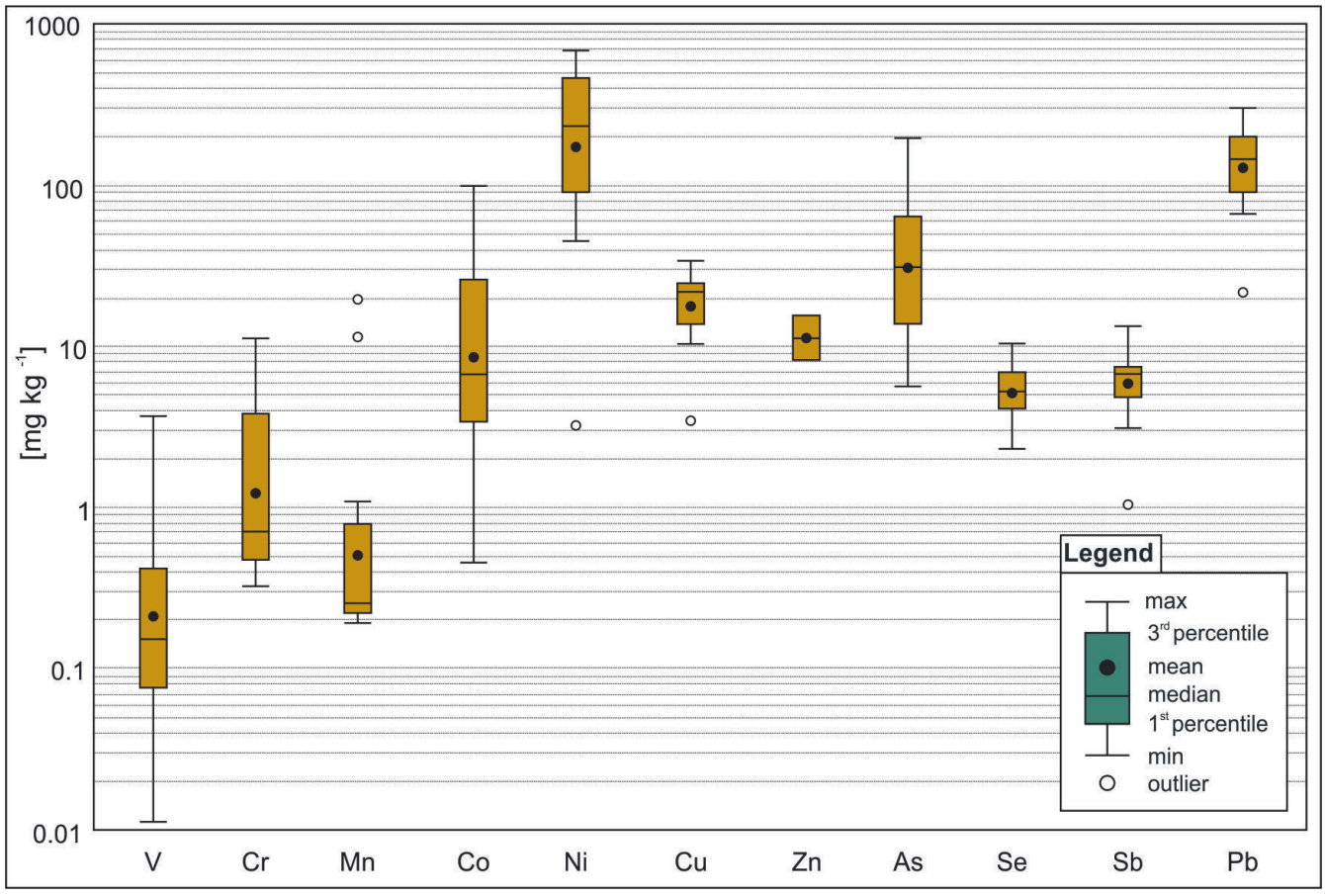

Figure 6: Box-and-whiskers plots illustrating the trace element composition of vein pyrite from the Carboniferous-Permian formation of the Karawanken tunnel. All data given in mg kg^{-1}.

Pyrite (n=16)	V	Cr	Mn	Co	Ni	Cu	Zn	As	Se	Sb	Hg	Te	Pb
Min	0.01	0.30	0.20	0.45	3.20	3.50	8.29	5.70	2.30	1.00	0.45	0.01	21.50
Mean	0.70	2.80	2.20	20.50	280	19.80	12.00	46.20	5.50	6.70	0.60	0.10	149
Median	0.15	0.71	0.26	6.80	240	21.80	12.00	31.00	5.30	6.80	0.60	0.08	147
Max	3.70	11.20	19.60	99.40	680	33.70	15.40	197	8.50	13.40	1.00	0.26	300
S.D.	1.20	4.00	29.00	28.50	218	8.00	5.00	46.80	2.00	3.00	0.20	0.07	72.60

Table 1: Statistical summary of vein-hosted pyrite geochemistry from the Karawanken tunnel. All data given in mg kg^{-1}.

Pyrite (n=3)	$\delta^{34}S$ value	Error
Kara-1s	+10.4 ‰	± 0.4
Kara-2s	+10.5 ‰	± 0.3
Kara-3s	+10.2 ‰	± 0.5

Table 2: Sulfur isotope composition ($\delta^{34}S$) of pyrite from Karawanken veins.

Pyrite	Co/Ni	Se/As	As/Sb
Min	0.01	0.04	0.92
Mean	0.09	0.09	8.29
Median	0.06	0.08	5.73
Max	0.50	0.15	31.32
S.D.	0.12	0.04	9.20

Table 3: Elemental ratios of pyrite from the Karawanken tunnel.

5. Discussion

5.1. Trace element constraints on pyrite formation

Pyrite can incorporate an array of trace elements through the mechanisms of crystal lattice substitutions or by including micro- to nanoscale particles of other minerals (e.g. Steadman et al., 2021). Some of these elements can provide valuable insights about its formation processes. Notably, selenium (Se) is a temperature-sensitive element exhibiting low solubility at lower temperatures but becoming readily available at temperatures exceeding 350 °C, irrespective of pH and fO_2 conditions (Revan et al., 2014; Keith et al., 2016; Maslennikov et al., 2020). The consistently low Se concentrations ranging from 2.30 to 8.50 mg kg^{-1} (median: 5.30 mg kg^{-1}) and remarkably low Se/As ratios (Tab. 3) (median: 0.08) strongly suggest a low-temperature origin (<350 °C) for the pyrite veins in the Karawanken tunnel (Reich et al., 2013).

5.2. Source of sulfur and sulfate reduction mechanisms

Geochemical processes involving living organisms or detrital organic matter have since long been used to explain the preferential enrichment of some metals in organic-rich sediments (Disnar and Sureau, 1990). Moreover, organic matter is also highly involved in the complexation, transport, and precipitation of various metals in hydrothermal systems, further supporting the notion that it is crucial to the formation and trace element enrichment in many types of ore deposits (e.g., Foltyn et al., 2022; Šoster et al., 2023 and references therein). Specific geological factors, such as deep burial, can lead to increased heat flow and the thermogenic breakdown of buried kerogen, resulting in the formation of hydrocarbons, notably methane and oil (e.g. Stolper et al., 2014). Generated hydrocarbons can subsequently participate in ore-forming systems as ligands and reducing agents.

The Carboniferous-Permian formations are known to contain pockets of methane (Buser, 1975; Budkovič, 1999; Ločniškar, 2022). The former occurs in such concentrations that it posed a safety risk, and special precautions had to be taken during tunnel construction (Ločniškar, 2022). Methane can be generated in multiple ways, for example by bacterial sulfate reduction (BSR), thermochemical sulfate reduction (TSR) or by thermochemical breakdown (cracking) of oil or detrital kerogen (Machel et al., 1995; Machel, 2001; Stolper et al., 2014). BSR and TSR occur in two mutually exclusive thermal regimes, whereas TSR overlaps with the production of thermogenic hydrocarbons (Machel et al., 1995; Stolper et al., 2014). The thermal maturity of organic matter, assessed by vitrinite reflectance measurements for Carboniferous-Permian rock formations in the Southern Karawanken range (Rantitch and Rainer, 2003), indicates peak diagenetic temperature conditions of 230 °C to 260 °C (Rainer et al., 2009; 2016). Within this temperature range, BSR reactions are unlikely to account for the generation of reduced sulfur (H_2S) and methane; instead, TSR is the prevailing mechanism.

The difference in sulfur isotope composition ($\delta^{34}S$) between sulfate and sulfide minerals ($\Delta\delta^{34}S$) is strongly temperature dependent. Machel et al. (1995) observed that during thermochemical sulfate reduction, predictable isotopic fractionation occurs at different temperatures: at 200°C, the $\Delta\delta^{34}S$ is 10 ‰, at 150 °C it is 15 ‰, and at 100 °C it reaches 20 ‰. Pyrite from the analyzed veins yielded uniformly positive values of sulfur isotopic composition ($\delta^{34}S$) with a median value of +10.4 ‰. While there are no specific data available regarding the sulfur isotopic composition of gypsum and anhydrite from the rocks in the Karawanken tunnel, $\delta^{34}S$ data on evaporites from the Carboniferous-Permian period in Central Slovenia can be considered as a proxy. These range from +16.5 to +19.2 ‰ (Drovenik et al., 1980), which is consistent with the global Phanerozoic seawater curve (+15.0 ‰) for the above-mentioned period (Claypool et al., 1980). The difference in the $\delta^{34}S$ of Carboniferous-Permian sulfide and sulfate minerals imply the degree of isotopic fractionation ($\Delta\delta^{34}S$) of ≈10 ‰. This aligns with peak diagenetic temperature conditions (>200 °C; Rainer et al., 2009; 2016) and reinforces the hypothesis of TSR as the primary mechanism for reduced sulfur and methane formation (e.g. Machel et al., 1995; Stolper et al., 2014).

5.3. Genetic model of the Karawanken pyrite veins

The geological sequence of the Karawanken tunnel consists of a thick and structurally complex sequence of Carboniferous to Late Triassic rocks which record the regional geological processes related to uplift of Alpine orogen. The pyrite veins in this sequence are hosted in organic-rich Carboniferous-Permian formation, which consists of black shale, sandstone and conglomerate intercalated by up to several meters' thick sequences of evaporites – namely anhydrite and gypsum (Buser, 1975; Ločniškar, 2022). The Carboniferous-Permian rocks are covered by a thick sequence of Mesozoic carbonates, reaching a total estimated stratigraphic thickness between 3000 and 5000 m (Buser, 1975). Rainer et al. (2009, 2016) used vitrinite reflectance as a temperature sensitive proxy to determine thermal maturity of sedimentary rocks in the Dinarides and Southern Alps. The vitrinite reflectance measurements of Late Carboniferous formations (Auernig Fm.) in the Southern Karawanken region ranged from 3.18 % to 4.88 %, indicating peak diagenetic temperatures of 230–260 °C. Additionally, vitrinite reflectance of solid bitumen from superimposed Mid- to Late Triassic rocks in this area correspond with temperatures of 190–220 °C (Rainer et al., 2016). The thermal alteration patterns observed are interpreted to be associated with the thickness of Cretaceous to Eocene flysch deposits. Following this thermal event, the rocks experienced cooling below 110 °C during the Late Eocene to Early Oligocene, while subsequent nappe stacking and compressional tectonic events did not further influence the thermal maturity of sedimentary rocks (Rainer et al., 2009, 2016). These temperatures (230–260 °C) are sufficient to facilitate the formation of thermogenic hydrocarbons (>150–160 °C) by breakdown (cracking) of oil and even detrital refractory kerogen (Clayton, 1991; Stolper et al., 2014). The organic matter present in Carboniferous-Permian sediments rocks was under these conditions thermally broken down to methane, which later acted as a reducing agent in the process of thermochemical sulfate reduction.

The primary source of available dissolved sulfate were evaporitic layers contained within Carboniferous-Permian rocks, as evidenced by the degree of sulfur isotope fractionation between sulfate and sulfide ($\Delta\delta^{34}S$ at 200 °C ≈10 ‰; Drovenik et al., 1980; Machel et al., 1995). The conversion of evaporitic SO_4^{2-} into H_2S occurred by the methane-mediated thermochemical reduction of sulfate. Furthermore, certain chemical elements, such as pyrite hosted Ni^{2+}, Fe^{2+} as well as clay mineral montmorillonite present in the host-rock, may have catalytically accelerated the rate of TSR (Machel, 2001).

Evaporites may have served not only as a source of sulfate but also played a significant role in the generation of mineralizing fluids. This is because the dehydration of gypsum, which occurs at T > 42 °C (Voigt and Freyer, 2023), leads to the release of substantial amounts of fluids. More importantly, phase transition does not occur instantly, but rather over an extended period (Voigt and Freyer, 2023), which explains co-occurrence of gypsum and anhydrite in the studied rocks. This dehydration, in turn, may lead to a rapid increase in pore pressure and an increase in porosity and permeability enabling fluid flow (Olgaard et al., 1995). The former mechanism likely played a significant role in creating pathways for mineral deposition, such as the formation of pyrite and later quartz-calcite veins. Additional evidence of evaporite dissolution are late-stage celestine-barite veinlets (Fig. 5; V4; Stage 5) intersecting pyrite and quartz-calcite veins (V3, V4). This occurs because during gypsum dissolution, Ba and Sr are selectively dissolved from the gypsum during the early stages of the process and may form corresponding sulfate minerals (Hanor, 2000).

The mineralizing fluid resulting from evaporite dissolution was probably low-chlorinity as pyrite as well as general mineral assemblage lacks base metals that are typically transported as metal-halogen complexes (e.g. Pb, Zn, Cu; Sverjensky, 1987; Yardley, 2005; Wood et al., 2006; Lukanin et al., 2013; Zhong et al., 2015; Yuan et al., 2021). The Co/Ni ratio of pyrite has traditionally been used to fingerprint deposit types and the origin of ore-forming fluids (e.g. Bralia et al., 1979; Craig et al., 1998; Clark et al., 2004; Feng et al., 2020). The values of the analyzed vein pyrite show very low Co/Ni ratio values (median: 0.06; Tab. 3) and plot well within the affinity field of typical sedimentary pyrite, indicating a significant metal input from the sediments (Fig. 7a) (Bralia et al., 1979; Raymond, 1996; Large et al., 2009; Feng et al., 2020). In addition, a wide range of Ni concentrations (3.20 to 683 mg kg^{-1}) further supports the notion of metal origin from sedimentary rocks, as pyrite precipitated from magmatic or magmatic-hydrothermal fluids commonly display significantly lower Ni concentrations than those observed in sedimentary rocks (Large et al., 2009; Gregory et al., 2015; Cafagna and Jugo, 2016; Shao et al., 2018).

The pyrite trace element characteristics of vein pyrite, such as Se concentrations and Se/As ratio suggest low-temperature origin of pyrite (<300–350 °C) (Reich et al., 2013; Revan et al., 2014; Keith et al., 2016; Maslennikov et al., 2020), which is consistent with the data inferred from sulfur isotope characteristics and peak diagenetic temperature conditions. We attempted to employ fluid inclusion geochemistry and thermometry in quartz and carbonate to constrain formation temperature of the hydrothermal cement. However, due to their small size (<10 um), the fluid inclusions were unsuitable for analysis under our microscope. In hydrothermal systems, pyrite typically forms from moderately reducing and pH neutral solutions, abundant in hydrogen sulfide (H_2S) and with smaller amounts of CO_2 (Wang et al., 2010; Lorand and Pont, 2022). The relationship between As and Sb may provide some insights into pH and redox conditions of an ore-forming fluid (e.g. Leuz et al., 2006; Hockmann et al., 2014; Ding et al., 2022). In natural environments, As^{3+} as $As(OH)_3$ is the predominant arsenic-bearing species over a wide temperature range (25–500 °C) (Pokrovski et al., 2002a; Pokrovski et al., 2002b; Perfetti et al., 2008). Conversely, antimony (Sb) is redox-sensitive, and its mobility strongly depends on redox conditions of the hydrothermal fluid (Leuz et al., 2006). In hydrothermal systems, antimony exists as two distinct species: $Sb(OH)_3$ under reducing and $Sb(OH)_5$ under oxidizing conditions (Mosley et al., 2014; Karimian et al., 2018). $Sb(OH)_3$ exhibits a pronounced preference for adsorption onto detrital Fe-oxide and hydroxide particles compared to $Sb(OH)_5$, thereby significantly limiting the mobility of antimony in reducing environments (Wan et al., 2013; Hockmann et al., 2014; Han et al., 2018). Consequently, under reducing conditions, As demonstrates heightened mobility relative to Sb, resulting in elevated As/Sb ratios (Leuz et al., 2006; Hockmann et al., 2014). The examined pyrite exhibits elevated As concentrations compared to Sb (Tab. 1), resulting in a wide range of As/Sb ratios (Tab. 3) (median: 5.7). This observation implies moderately reducing conditions during the precipitation of pyrite.

5.4. Environmental considerations

The investigated pyrite-rich segment within the Carboniferous-Permian formation of the Karawanken Tunnel occupies a relatively narrow, likely fault-controlled zone within an otherwise impermeable siliciclastic rock formation. This suggests that the rock formation may possess self-limiting capabilities, physically preventing the lateral and vertical mobility of possible acidic discharge coming from pyrite oxidation. Additionally, the impermeable Paleozoic clastic sequences in this region are not considered aquifers as the primary water supply is predominantly sourced from fractured-karst type aquifers (Brenčič and Polting, 2008). Due to their occurrence in carbonates, which exhibit acid buffering capacity, fractured-karst type aquifers are capable of neutralizing potential acidic discharges and facilitating the precipitation of potentially toxic elements, removing them from groundwater. *In-vitro* studies have also demonstrated that neutralization by calcium carbonate (e.g. limestone) can reduce the concentration of heavy metals in solution by up to 94 % within a short period of time (e.g. Fan et al., 2016; Zhang et al., 2023). Furthermore, the analyzed pyrite generally exhibits low concentrations of potentially toxic chemical elements such as As, Cu, Pb, Sb, and Hg (Table 1), contrasting sharply with the heavy load of these elements found in pyrite derived from polymetallic mining activities (Fan et al., 2016; Steadman et al., 2021; Lorand and Pont, 2022; Mederski et al., 2022;). This characteristic significantly reduces the risk of environmental contamination. From an engineering perspective, the occurrence of pyrite was addressed through the use of

acid- and sulfate-resistant concrete mixtures, designed to prevent potential corrosion resulting from the oxidation of pyrite.

6. Conclusions

The pyrite veins within the Karawanken tunnel are hosted in highly deformed, organic-rich Carboniferous-Permian shales. These veins underwent three distinct deformation phases: parallel, perpendicular, and oblique to the bedding planes, each associated with unique hydrothermal cements. Overlying these formations is a thick sequence of Mesozoic carbonates, with a total stratigraphic thickness estimated between 3000 and 5000 meters. This significant overburden induced thermal alteration, with peak diagenetic temperatures reaching 230 to 260 °C. At these temperatures, the organic matter within the shales thermally decomposed into methane, which subsequently participated in sulfate reduction. The primary sulfate source derived from evaporitic layers within the Carboniferous-Permian formations. Methane-mediated thermochemical sulfate reduction facilitated the conversion of evaporitic sulfate into H_2S. Additionally, the presence of some cations (e.g. Ni^{2+}, Fe^{2+}) and clay minerals (montmorillonite) might have catalyzed the rates of sulfate reduction. Mineralizing fluids originated from the expulsion of interstitial waters in sediments, and likely augmented by the dissolution and phase transition (dehydration) between gypsum and anhydrite. The geochemical data indicate metal origin from the sedimentary rocks. These pyrite forming fluids were characterized by low temperature (<300–350 °C), moderate reducing conditions, and low chlorinity. The potential environmental impact of pyrite is mitigated by the fine-grained, impermeable siliciclastic nature of the host rock, which physically restricts the mobility of potential acidic discharge from pyrite oxidation. Additionally, the low concentration of potentially toxic elements in the vein pyrite further reduces the risk of pollution and environmental impact.

Acknowledgements

This paper is a contribution to the International Geoscience Program (IGCP) Project 683 – "Pre-Atlantic geological connections among northwest Africa, Iberia and eastern North America: Implications for continental configurations and economic resources". The authors acknowledge the financial support from the Slovenian Research and Innovation Agency (ARIS) via program group P1-0195 "Geoenviromnent and Geomaterials". We thank dr. M. Velojić (University of Belgrade, Faculty of Mining and Geology, Serbia) for the assessment of fluid inclusion samples. The authors gratefully acknowledge the valuable comments and suggestions provided by the two reviewers, which contributed to the quality of the manuscript.

References

Bauer F.K., 1981. Geologische Karte der Ostkarawanken 1:25 000, Ostteil, 3 Blätter. Geologische Bundesanstalt, Wien.

Bralia A., Sabatini G., Troja F., 1979. A revaluation of the Co/Ni ratio in pyrite as geochemical tool in ore genesis problems. Mineralium Deposita 14, 353–374. https://doi.org/10.1007/BF00206365

Brandão Capraro A.P., Macioski G., de Medeiros M.H.F., 2021. Effect of aggregate contamination with pyrite on reinforcement corrosion in concrete. Engineering Failure Analysis 120, 105116. http://doi.org/10.1016/j.engfailanal.2020.105116

Brenčič M., Polting,W., 2008. Grundwasser der Karawanken – Versteckter Schatz = Pozdemne vode Karavank – Skrito bogastvo. Geological Survey of Slovenia, Joanneum Research Forschungsgesellschaft m.b.h., Ljubljana, Graz, 143 pp.

Budkovič T., 1999. Geology of the Slovene part of the Karavanke road tunnel. Abhandlungen der Geologischen Bundesanstalt 56/2, 35–48.

Buggisch W., 1987. Die Grödener Schischten (Perm, Südalpen). Sedimentologische und geokemische Untersuchungen zur Unterscheidung mariner und kontinentaler Sedimente. Geologische Rundschau 67, 149–180.

Buser S., 1975. Basic Geological Map of Socialist Federative Republic of Yugoslavia 1:100 000 – Interpretation of sheet Celovec. Federal Geological Survey Belgrade (Belgrade), 1–62. (in Slovenian).

Cafagna F., Jugo P.J., 2016. An experimental study on the geochemical behavior of highly siderophile elements (HSE) and metalloids (As, Se, Sb, Te, Bi) in a mss-iss-pyrite system at 650 °C: A possible magmatic origin for Co-HSE-bearing pyrite and the role of metalloid-rich phases in the fractionation of HSE. Geochimica et Cosmochimica Acta 178, 233–258. https://doi.org/10.1016/j.gca.2015.12.035

Clark C., Grguric B., Mumm Schmidt A., 2004. Genetic implications of pyrite chemistry from the Palaeoproterozoic Olary Domain and overlying Neoproterozoic Adelaidean sequences, northeastern South Australia. Ore Geology Reviews 25/3–4, 237–257. https://doi.org/10.1016/j.oregeorev.2004.04.003

Claypool G.E., Holser W.T., Kaplan I.R., Sakai H., Zak I., 1980. The age curves of sulfur and oxygen isotopes in marine sulfate and their mutual interpretation. Chemical Geology 28, 199–260. https://doi.org/10.1016/0009-2541(80)90047-9

Clayton C., 1991. Carbon isotope fractionation during natural gas generation from kerogen. Marine and Petroleum Geology 8/2, 232–240. https://doi.org/10.1016/0264-8172(91)90010-X

Cook N., Ciobanu C.L., George L., Zhu Z.-Y., Wade B., Ehrig K., 2016. Trace Element Analysis of Minerals in Magmatic-Hydrothermal Ores by Laser Ablation Inductively-Coupled Plasma Mass Spectrometry: Approaches and Opportunities. Minerals 6/4, 111. https://doi.org/10.3390/min6040111

Craig J.R., Vokes F.M., Solberg T.N., 1998. Pyrite: physical and chemical textures. Mineralium Deposita 31/1, 82–101. https://doi.org/10.1007/s001260050187

DARS. Predor Karavanke – vzhodna cev. https://www.dars.si/Infrastrukturni_projekti/Predor_Karavanke_-_druga_cev (accessed on 06. June 2024)

Ding T., Tan T., Wang J., Ma D., Lu J., Zhang R., Liang J., 2022. Trace-element composition of pyrite in the Baoshan Cu-Mo-Pb-Zn deposit, southern Hunan Province, China: Insights into the ore genesis. Ore Geology Reviews 147, 104989. https://doi.org/10.1016/j.oregeorev.2022.104989

Disnar J.R., Sureau J.F., 1990. Organic matter in ore genesis: Progress and perspectives. Organic Geochemistry 16/1–3, 577–599. https://doi.org/10.1016/0146-6380(90)90072-8

Dozet S., Buser S., 2009. In: Pleničar M., Ogorelec B., Novak M. (eds.), The Geology of Slovenia. Geological Survey of Slovenia, Ljubljana, 161–214.

Drovenik M., Pleničar M., Drovenik F., 1980. The origin of Slovenian ore deposits. Geologija 23/1, 1–157.

Ebner F., Vozárová A., Kovács S., Kräutner H.G., Krstić B., Szederkenyi T., Jamićić D., Balen D., Belak M., Trajanova M., 2008. Devonian-Carboniferous pre-flysch and flysch environments in the Circum Panonian Region. Geologica Carpathica 59, 159–195.

Evangelou V.P.B., Zhang Y.L., 1995. A review: Pyrite oxidation mechanisms and acid mine drainage prevention. Critical Reviews in Environmental Science and Technology 25/2, 141–199. https://doi.org/10.1080/10643389509388477

Fan L., Zhou X., Luo H., Deng J., Dai L., Ju Z., Zh Z., Zou L., Ji L., Cheng L., 2016. Release of Heavy Metals from the Pyrite Tailings of Huangjiagou Pyrite Mine: Batch Experiments. Sustainability 8/1, 96. https://doi.org/10.3390/su8010096

Farabegoli E., Flügel E., Levanti D., Noe S., Pasini M., Perri M.C., Venturini C., 1986. The Traviso Breccia and Val Gardena Sandstone: Lithostratigraphy and Paleoenvironments. The Permian/Triassic boundary - Carnic and Comelico. In: Field Conference on Permian/Triassic Boundary in the South-Alpine Segment of the Western Tethys. Excursion Guidebook. Societá Geologica Italiana, Commerciale Pavese, Pavia, 55–72.

Feng Y., Zhang Y., Xie Y., Shao Y., Lai C., 2020. Pyrite geochemistry and metallogenic implications of Gutaishan Au deposit in Jiangnan Orogen, South China. Ore Geology Reviews 117, 103298. https://doi.org/10.1016/j.oregeorev.2019.103298

Foltyn K., Bertrandsson Erlandsson V., Zygo W., Melcher F., Pieczonka J., 2022. New perspective on trace element (Re, Ge, Ag) hosts in the Cu-Ag Kupferschiefer deposit, Poland: Insight from a LA-ICP-MS trace element study. Ore Geology Reviews 143, 104768. https://doi.org/10.1016/j.oregeorev.2022.104768

Gregory D.D., Large R.R., Halpin J. A., Lounejeva Baturina E.L., Lyons T.W., Wu S., Danyushevsky L., Sack P.J., Chappaz A., Maslennikov V.V., Bull S.W., 2015. Trace Element Content of Sedimentary Pyrite in Black Shales. Economic Geology 110/6, 1389–1410. https://doi.org/10.2113/econgeo.110.6.1389

Han Y.-S., Seong H.S., Chon C.-M., Park J.H., Ham I.-J., Yoo K., Ahn J.S., 2018. Interaction of Sb(III) with iron sulfide under anoxic conditions: Similarities and differences compared to As(III) interactions. Chemosphere 195, 762–770. https://doi.org/10.1016/j.chemosphere.2017.12.133

Hanor J.S., 2000. Barite-Celestine Geochemistry and Environments of Formation. Reviews in Mineralogy and Geochemistry 40/1, 193–275. https://doi.org/10.2138/rmg.2000.40.4

Hockmann K., Lenz M., Tandy, S., Nachtegaal M., Janousch M., Schulin R., 2014. Release of antimony from contaminated soil induced by redox changes. Journal of Hazardous Materials 275, 215–221. https://doi.org/10.1016/j.jhazmat.2014.04.065

Karimian N., Johnston S.G., Burton E.D., 2018. Antimony and arsenic partitioning during Fe2+-induced transformation of jarosite under acidic conditions. Geosphere 195, 515–523. https://doi.org/10.1016/j.chemosphere.2017.12.106

Keith M., Haase K.M., Klem R., Krumm S, Strauss H., 2016. Systematic variations of trace element and sulfur isotope compositions in pyrite with stratigraphic depth in the Skouriotissa volcanic-hosted massive sulfide deposit, Troodos ophiolite, Cyprus. Chemical Geology 423, 7–18. https://doi.org/10.1016/j.chemgeo.2015.12.012

Krainer K., 1992. Facies, sedimentationsprozesse und paläogeographie im Karbon der Ost- und Süd Alpen. Jahrbuch der Geologischen Bundesanstalt 135, 87–99.

Krainer K., 1993. Late- and post-Variscan sediments of the Eastern and Southern Alps. In. von Raumer J.F., Neubauer F. (Eds.): Pre-Mesozoic Geology in the Alps. Monograph, Springer Verlag, 537–564.

Large R.R., Danyushevsky L., Hollit C., Maslennikov V., Meffre S., Gilbert S., Bull S., Scott R., Emsbo P., Thomas H., Singh B., Foster J., 2009. Gold and Trace Element Zonation in Pyrite Using a Laser Imaging Technique: Implications for the Timing of Gold in Orogenic and Carlin-Style Sediment-Hosted Deposits. Economic Geology 104/5, 635–668. https://doi.org/10.2113/gsecongeo.104.5.635

Large R.R., Meffre S., Burnett R., Guy B., Bull S., Glibert S., Goemann K., Danyushevsky L., 2013. Evidence for an Intrabasinal Source and Multiple Concentration Processes in the Formation of the Carbon Leader Reef, Witwatersrand Supergroup, South Africa. Economic Geology 108/6, 1215–1241. https://doi.org/10.2113/econgeo.108.6.1215

Leuz A.K., Monch H., Johnson C.A., 2006. Sorption of Sb(III) and Sb(V) to goethite: influence on Sb(III) oxidation and mobilization. Environmental Science and Technology 40/23, 7277–7280. https://doi.org/10.1021/es061284b

Liang X., Li B., Zhang X., Qin H., Li G., 2024. Fluid mixing, organic matter, and the origin of Permian carbonate-hosted Pb-Zn deposits in SW China: New Insights from the Fuli deposit. Minerals 14/3, 312. https://doi.org/10.3390/min14030312

Liao X., Zhang W., Chen J., Wang Q., Wu X., Ling S., Guo D., 2020. Deterioration and Oxidation Characteristics of Black Shale under Immersion and Its Impact on the Strength of Concrete. Materials 13/11, 2515. https://doi.org/10.3390/ma13112515

Ločniškar A., 2022. Predor Karavanke – 30 let pozneje. In: Rman N., Bračič Železnik B., Žvab Rožič P. (eds.), Proceedings of the 6th Slovenian geological congress – Book of abstracts, 3rd–5th October 2022, Rogaška Slatina. Slovenian Geological Society, Ljubljana,14. (in Slovenian)

Lorand J.-P., Pont S., 2022. Tl-rich pyrite and Sb-rich melnikovite in Montlouis pyrite veins (Central Armorican domain, Janze, Ille-et-Vilaine; France). Comptes Rendus Géoscience 354/G2, 303–317. https://doi.org/10.5802/crgeos.143

Lukanin O.A., Ryzhenko B.N., Kurovskaya N.A., 2013. Zn and Pb solubility and speciation in aqueous chloride fluids at T-P parameters corresponding to granitoid magma degassing and crystallization. Geochemistry International 51, 802–830. https://doi.org/10.1134/S0016702913090048

Machel H.G., Krouse H.R., Sassen R., 1995. Products and distinguishing criteria of bacterial and thermochemical sulfate reduction. Applied Geochemistry 10/4, 373–389. https://doi.org/10.1016/0883-2927(95)00008-8

Machel H.G., 2001. Bacterial and thermochemical sulfate reduction in diagenetic settings – old and new insights. Sedimentary Geology 140/1–2, 143–175. https://doi.org/10.1016/S0037-0738(00)00176-7

Maslennikov V.V., Cherkashov G., Artemyev D.A., Firstova A., Large R.R., Tseluyko A., Kotlyarov V., 2020. Pyrite varieties at Pobeda hydrothermal fields, Mid-Atlantic Ridge 17°07´–17°08´ N: LA-ICP-MS data deciphering. Minerals: 10/7, 622. https://doi.org/10.3390/min10070622

Mederski S., Pršek J., Majzlan J., Kieferm S., Dimitrova D., Milovský R., Bender Koch C., Kozień D., 2022. Geochemistry and textural evolution of As-Tl-Sb-Hg-rich pyrite from a sediment-hosted As-Sb-Tl-Pb ± Hg ± Au mineralization in Janjevo, Kosovo. Ore Geology Reviews 151, 105221. https://doi.org/10.1016/j.oregeorev.2022.105221

Mosley L.M., Shand P., Self P., Fitzpatrick R., 2014. The geochemistry during management of lake acidification caused by the rewetting of sulfuric (pH < 4) acid sulfate soils. Applied Geochemistry 41, 49–61. https://doi.org/10.1016/j.apgeochem.2013.11.010

Novak M., 2007. Depositional environment of Upper Carboniferous – Lower Permian in Karavanke Mountains (Southern Alps, Slovenia). Geologija 50/2, 247–268. https://doi.org/10.5474/geologija.2007.018

Novak M., Skaberne D., 2009. Upper Carboniferous and Lowe Permian. In: Pleničar M., Ogorelec B., Novak M. (eds.), The Geology of Slovenia. Geological Survey of Slovenia, Ljubljana, 99–136.

Novak M., Krainer K., 2022. The Rigelj Formation, a new lithostratigraphic unit of the Lower Permian in the Karavanke Mountains (Slovenia/Austria). Austrian Journal of Earth Sciences 115, 100–123. https://doi.org/10.17738/ajes.2022.0005

Ogorelec B., 2011. Microfacies of Mesozoic Carbonate Rocks of Slovenia. Geologija 54/2, 1–135. https://doi.org/10.5474/geologija.2011.011

Olgaard L.D., Ko S.-C., Wong T.-F., 1995. Deformation and pore pressure in dehydrating gypsum under transiently drained conditions. Tectonophysics 245/3–4, 237–248. https://doi.org/10.1016/0040-1951(94)00237-4

Onuk P., Melcher F., Mertz-Kraus R., Gäbler H.-E., Goldmann S., 2017. Development of a matrix-matched sphalerite reference material (MUL-ZnS-1) for calibration of in situ trace element measurements by laser ablation-inductively coupled plasma-mass spectrometry. Geostandards and Geoanalytical Research 41/2, 263–272. https://doi.org/10.1111/ggr.12154

Ori G.G., Venturini C., 1981. Facies continentali permiane nelle Alpi Carniche. Rendiconti Societá Geologica Italiana 3, 21–24.

Panton C., Hellstrom J., Paul B., Woodhead J., Hergt J., 2011. Iolite: Freeware for the visualisation and processing of mass spectrometric data. Journal of Analytical Atomic Spectroscopy 26/12, 2508. https://doi.org/10.1039/C1JA10172B

Passchier C.W., Trouw R.A.J., 2005. Microtectonics, second ed. Springer Berlin, Heidelberg, 382. https://doi.org/10.1007/3-540-29359-0

Perfetti E., Pokrovski G.S., Ballerat-Busserolles K., Majer V., Gilbert F., 2008. Densities and heat capacities of aqueous arsenious and arsenic acid solutions to 350 °C and 300 bar, and revised thermodynamic properties of As(OH)3°(aq), AsO(OH)3°(aq) and iron sulfarsenide minerals. Geochimica et Cosmochimica Acta 72/3, 713–731. https://doi.org/10.1016/j.gca.2007.11.017

Placer L., 2008. Principles of tectonic subdivision of Slovenia. Geologija 51/2, 205–217. https://doi.org/10.5474/geologija.2008.021

Pokrovski G.S., Zakirov I.L., Roux J., Testemale D., Hazemann J.-L., Bychkov A.Y., Golikova G.V., 2002a. Experimental study of arsenic speciation in vapor phase to 500°C: Implications for As transport and fractionation in low-density crustal fluids and volcanic gases. Geochimica et Cosmochimica Acta, 66/19, 3453–3480. https://doi.org/10.1016/S0016-7037(02)00946-8

Pokrovski G.S., Kara S., Roux J., 2002b. Stability and solubility of arsenopyrite, FeAsS, in crustal fluids. Geochimica et Cosmochimica Acta 66/13, 2361–2378. https://doi.org/10.1016/S0016-7037(02)00836-0

Rainer T., Sachsenhofer R.F., Rantitsch G., Herlec U., Vrabec M., 2009. Organic maturity trends across the Variscan discordance in the Alpine-Dinaric Transition Zone (Slovenia, Austria, Italy): Variscan versus Alpidic thermal overprint. Austrian Journal of Earth Sciences 102/2, 120–133.

Rainer T., Sachsenhofer R.F., Green P.F., Rantitsch G., Herlec U., Vrabec M., 2016. Thermal maturity of Carboniferous to Eocene sediments of the Alpine-Dinaric transition zone (Slovenia). International Journal of Coal Geology 157, 19–38. https://doi.org/10.1016/j.coal.2015.08.005

Ramovš A., 1958. O faciesih v zgornjem wordu in zgornjem permu v Sloveniji. Geologija 4, 75–78.

Raymond O.L., 1996. Pyrite composition and ore genesis in the Prince Lyell copper deposit, Mt Lyell mineral field, western Tasmania, Australia. Ore Geology Reviews 10/3–6, 231–250. https://doi.org/10.1016/0169-1368(95)00025-9

Reich M., Deditius A., Chryssoulis S., Li J.-W., Ma C.-Q., Parada M.A., Barra F., Mittermayr F., 2013. Pyrite as a record of hydrothermal fluid evolution in a porphyry copper system: A SIMS/EMPA trace element study. Geochimica et Cosmochimica Acta 104, 42–62. https://doi.org/10.1016/j.gca.2012.11.006

Rantitsch G., Rainer T., 2003. Thermal modeling of Carboniferous to Triassic sediments of the Karawanken Range (Southern Alps) as a tool for paleogeographic reconstructions in the Alpine-Dinaridic-Pannonian realm. International Journal of Earth Sciences 92/2, 195–209. https://doi.org/10.1007/s00531-003-0312-4

Revan M.K., Genç Y., Maslennikov V.V., Maslennikova S.P., Large R.R., Danyushevsky L.V., 2014. Mineralogy and trace-element geochemistry of sulfide minerals in hydrothermal chimneys from the Upper-Cretaceous VMS deposits of the eastern Pontide orogenic belt (NE Turkey). Ore Geology Reviews 63, 129–149. https://doi.org/10.1016/j.oregeorev.2014.05.006

Schmid S.M., Fügenschuh B., Kounov A., Maţenco L., Nievergelt P., Oberhänsli R., Pleuger J., Schefer S., Schuster R., Tomljenović B., Ustaszewski K., van Hinsbergen D.J.J., 2020. Tectonic units of the Alpine collision zone between Eastern Alps and western Turkey. Gondwana Research 78, 308–374. https://doi.org/10.1016/j.gr.2019.07.005

Shao Y.-J., Wang W.-S., Liu Q.-Q., Zhang Y., 2018. Trace Element Analysis of Pyrite from the Zhengchong Gold Deposit, Northeast Hunan Province, China: Implications for the Ore-Forming Process. Minerals 8/6, 262. https://doi.org/10.3390/min8060262

Skaberne D., Ramovš A., Ogorelec B., 2009. Middle and Upper Permian. In: Pleničar M., Ogorelec B., Nova M. (eds.), The Geology of Slovenia. Geological Survey of Slovenia, Ljubljana, 137–154.

Stampfli G.M., Hochard C., Vérard C., Wilhem C., von Raumer J., 2013. The formation of Pangea. Tectonophysics 593, 1–19. https://doi.org/10.1016/j.tecto.2013.02.037

Steadmann J.A., Large R.R., Olin P.H., Danyushevsky L.V., Meffre S., Huston D., Fabris A., Lisitsin V., Wells T., 2021. Pyrite trace element behavior in magmatic-hydrothermal environments: An LA-ICPMS imaging study. Ore Geology Reviews 128, 103878. https://doi.org/10.1016/j.oregeorev.2020.103878

Stolper D.A., Lawson M., Davis C.L., Ferreira A.A., Santos Neto E.V., Ellis G.S., Lewan M.D., Martini A.M., Tang Y., Schoell M., Sessions A.L., Eiler J.M., 2014. Formation temperatures of thermogenic and biogenic methane. Science 344/6191, 1500–1503. https://doi.org/10.1126/science.1254509

Sverjensky D.A., 1987. The role of migrating oil field brines in the formation of sediment-hosted Cu-rich deposits. Economic Geology 82/5, 1130–1141. https://doi.org/10.2113/gsecongeo.82.5.1130

Šoster A., Bertrandsson Erlandsson V., Velojić M., Gopon P., 2023. Ultraviolet-photoluminescence and trace element analyses in Ga-rich sphalerite from the Djebel Gustar Zn-Pb deposit, Algeria. Ore Geology Reviews 157, 105474. https://doi.org/10.1016/j.oregeorev.2023.105474

Tribovillard N., Algeo T.J., Lyons T., Riboulleau A., 2006. Trace metals as paleoredox and paleoproductivity proxies: An update. Chemical Geology 232/1–2, 12–32. https://doi.org/10.1016/j.chemgeo.2006.02.012

Tu Z., W Q., He, H., Zhou S., Liu J., He H., Liu C., Dang Z., Reinfelder J.R., 2022. Reduction of acid mine drainage by passivation of pyrite surfaces: A review. Science of The Total Environment 832, 155116. https://doi.org/10.1016/j.scitotenv.2022.155116

Voigt W., Freyer D., 2023. Solubility of anhydrite and gypsum at temperatures below 100°C and the gypsum-anhydrite transition temperature in aqueous solutions: a re-assessment. Frontiers in Nuclear Engineering 2, 1208582. https://doi.org/10.3389/fnuen.2023.1208582

Vozárová A., Ebner F., Kovács S., Kräutner H.-G., Szederkenyi T., Krstić B., Sremac S., Aljinovič D., Novak M., Skaberne D., 2009. Late Variscan (Carboniferous to Permian) environments in the Circum Pannonian Region. Geologica Carpathica 60/1, 71–104. https://doi.org/10.2478/v10096-009-0002-7

Wan X.-M., Tandy S., Hockmann K., Schulin R., 2013. Changes in Sb speciation with waterlogging of shooting range soils and impacts on plant uptake. Environmental Pollution 172, 53–60. https://doi.org/10.1016/j.envpol.2012.08.010

Wang D., Wang Q., Wang T., 2010. Shape controlled growth of pyrite FeS2 crystallites via a polymer-assisted hydrothermal route. CrystEngComm 12, 3797–3805. https://doi.org/10.1039/C004266H

Wilson S.A., Ridley W.I., Koenig A.E., 2002. Development of sulfide calibration standards for the laser ablation inductively-coupled plasma mass spectrometry technique. Journal of Analytical Atomic Spectrometry 17, 406–409. https://doi.org/10.1039/b108787h

Wood S.A., Samson I.M., 2006. The aqueous geochemistry of gallium, germanium, indium and scandium. Ore Geology Reviews 28/1, 57–102. https://doi.org/10.1016/j.oregeorev.2003.06.002

Yardley B.W.D., 2005. Metal Concentrations in Crustal Fluids and Their Relationship to Ore Formation. Economic Geology 100/4, 613–632. https://doi.org/10.2113/gsecongeo.100.4.613

Yuan W., Chen J., Teng H., Chetelat B., Cai H., Liu J., Wang Z., Bouchez J., Moynier F., Gaillardet J., Schott J., Liu C., 2021. A review on the elemental and isotopic geochemistry of gallium. Global Biogeochemical Cycles 35/9, e2021GB007033. https://doi.org/10.1029/2021GB007033

Zhang Y., Fang Q., Lv J., Fu Y., Zhu J., Peng G., Li M., Wu X., Wang H., Chen Z., 2023. Source control on the acid mine drainage produced by the oxidation of pyrite and sulfur-containing uranium tailings based on the microbially induced carbonate precipitation technology. Journal of Cleaner Production 428, 139444. https://doi.org/10.1016/j.jclepro.2023.139444

Zhong R., Brugger J., Chen Y., Li W. 2015. Contrasting regimes of Cu, Zn and Pb transport in ore-forming hydrothermal fluids. Chemical Geology 395, 154–164. https://doi.org/10.1016/j.chemgeo.2014.12.008

Received: 8.7.2024
Accepted: 1.10.2024
Editorial Handling: Bastian Joachim-Mrosko